Journal of Materials Chemistry A

Dual functions of CO2 molecular activation and 4f levels as electron transport bridge in erbium single atom composite photocatalysts therefore enhancing visible-light photoactivities

Journal:	*Journal of Materials Chemistry A*
Manuscript ID	TA-ART-04-2021-002926.R1
Article Type:	Paper
Date Submitted by the Author:	28-May-2021
Complete List of Authors:	Chen, Qiuyu; Heilongjiang University; Environmental Monitoring Station of Qiqihar Gao, Guoyang; Heilongjiang University Zhang, Yanzhou; Heilongjiang University Li, Yini; Heilongjiang University Zhu, Hongyang; Linyi University, a. School of Physics and Electronic Engineering Zhu, Peifen; the University of Tulsa, Department of Physics and Engineering Physics Qu, Yang; Heilongjiang University, ; Key Laboratory of Functional Inorganic Materials Chemistry (Heilongjiang University), Ministry of Education, School of Chemistry and Materials Science, International Joint Research Center for Catalytic Technology, Harbin 150080, P. R. China., Wang, Guofeng; Heilongjiang University, Qin, Weiping; State Key Laboratory on Integrated Optoelectronics, College of Electronic Science and Engineering, Jilin University

ARTICLE

Dual functions of CO_2 molecular activation and 4*f* levels as electron transport bridge in erbium single atom composite photocatalysts therefore enhancing visible-light photoactivities

Received 00th January 20xx,
Accepted 00th January 20xx

DOI: 10.1039/x0xx00000x

Qiuyu Chen,[‡a] Guoyang Gao,[‡a] Yanzhou Zhang,[a] Yini li,[a] Hongyang Zhu,*[b] Peifen Zhu,[c] Yang Qu,[a] Guofeng Wang*[a] and Weiping Qin[d]

Only when the interfacial charge separation is enhanced and the CO_2 activation is improved, can the heterojunction nanocomposite photocatalyst be brought into full play for CO_2 reduction reaction (CO_2RR). Here, Er^{3+} single atom composite photocatalysts were successfully constructed based on both the special role of Er^{3+} single atom and the special advantages of $SrTiO_3$:Er^{3+}/g-C_3N_4 heterojunction in the field of photocatalys is for the first time. As we expected, the $SrTiO_3$:Er^{3+}/g-C_3N_4 (22.35 and 16.90 μmol g^{-1} h^{-1} for CO and CH_4) exhibits about 5 times enhancement in visible-light photocatalytic capability compared to pure g-C_3N_4 (4.60 and 3.40 μmol g^{-1} h^{-1} for CO and CH_4). In particular, the photocatalytic performance of $SrTiO_3$:Er^{3+}/g-C_3N_4 is more than three times higher than that of $SrTiO_3$/g-C_3N_4. From Er^{3+} fluorescence quenching, photoelectrochemistry, transient PL and DFT calculation, it is verified that a small fraction of surface doping of Er^{3+} formed Er single-atoms on $SrTiO_3$ building acted as an energy transfer bridge between the interface of $SrTiO_3$ and g-C_3N_4, resulting in the enhanced interfacial charge separation. Aberration-corrected high-angle annular dark-field scanning transmission electron microscopy (AC HAADF-STEM) and adsorption energy calculations demonstrated that the exposed Er single-atoms outside interface on $SrTiO_3$ is preferentially activate the adsorbed CO_2, leading to the high photoactivity for CO_2RR. A novel enhanced photocatalytic mechanism was proposed, in which dual effects of Er single-atoms act as an energy transfer bridge and realize CO_2 activation to promote charge separation. This provides new insights and feasible routes to developing highly efficient photocatalytic materials by engineering rare-earth single-atom doping.

1. Introduction

The photocatalytic CO_2 reduction (CO_2RR) with the use of solar energy has been extensively investigated over the past few years because it can not only solve the greenhouse effect of CO_2 but also convert CO_2 into fuels or other valuable chemical products.[1-4] So far, various photocatalysts have been employed in different types of photocatalysis processes, including photodegradation, H_2 evolution and CO_2 reduction et al.[5-8] however, new photocatalytic materials with enhanced charge separation and CO_2 activation are highly desired due to the compared low efficiency at present.[9-11]

Graphitic carbon nitride (g-C_3N_4) as one of the metal-free polymeric semiconductors has the advantages of the appropriate bandgap for absorbing solar energy, very negative conduction band (CB) potential (-1.1 eV) for reduction, low cost and environmental friendliness.[12-17] However, the high charge recombination rate prevents the high photocatalytic activity. Additionally, because there is no metal, the surface catalytic capacity of CN is poor, especially for CO_2RR.[18-19] Many approaches have been utilized to improve the photocatalytic performance of CN.[20-22] Among them, coupling with other materials to construct type II heterojunction nanocomposite has been proven as one of the most efficient methods.[23-27] However, it is an energy lost process for the photoelectrons in type II heterojunctions, although the charge separation is enhanced.[28] On the consideration of maintaining the thermodynamic energy of photoelectrons from CN, the CB of the coupled semiconductor should be as negative as possible. $SrTiO_3$ (STO) with negative CB (-0.71 eV) and highly stable has been regarded as an ideal candidate to couple with CN for photocatalytic CO_2RR.[29] However, the mismatched interface of STO/CN suppresses the charge transfer across the heterogeneous interface and the poor CO_2 activation further reduce the photoactivity.

As for improving the quality of interface, an electron transfer bridge achieved by employing noble metals such as Au, Ag, and carbon materials like graphene is confirm to be effective. However, the higher price, complicated operation and instability restrict their application in photocatalysis. In recent

[a] *Key Laboratory of Functional Inorganic Material Chemistry, Ministry of Education, School of Chemistry and Materials Science, Heilongjiang University, Harbin 150080, China. E-mail: 2010070@hlju.edu.cn*
[b] *School of Physics and Electronic Engineering, Linyi University, Linyi 276005, China. E-mail: zhuhongyang@lyu.edu.cn*
[c] *Department of Physics and Engineering Physics, The University of Tulsa, Tulsa, OK 74104, USA.*
[d] *College of Electronic Science and Engineering, Jilin University,Changchun 130012, China.*

†Electronic Supplementary Information (ESI) available: [details of any supplementary information available should be included here]. See DOI: 10.1039/x0xx00000x

‡Qiuyu Chen and Guoyang Gao contributed equally to this work.

years, it has been widely concerned that single-atom catalysts (SACs) played a huge role due to their maximized atom utilization and tunable electronic properties.[30-35] In particular the rare earth (RE) single-atom ones displayed promoted activity for CO_2RR due to their unique 4f electronic structure.[36-38] Therefore, it is desirable to introduce RE single-atoms in the interface of STO/CN nanocomposite. To the best of our knowledge, there is little works focused on this point which may due to the lack of an efficient method for preparing RE single-atoms.

Depending on the electronic band structure, STO is the photoelectrons accepter and the substrate of the consequent reduction for CO_2RR. Since the activation by photogenerated electrons occurs on STO, the activation and surface catalytic capacity of CO_2 is of significance. Coincidentally, owing to the abundant f electronic structure and strong affinity to CO_2, RE single-atoms are regarded as the great candidate for CO_2RR by the separated photogenerated electrons. Recently, our group has developed an in-situ doping method for preparing RE single-atoms with tunable dispersion density, and the promoted photocatalytic CO_2RR activities were achieved, especially for the Er single-atoms.[36] Thus, modifying RE single-atoms like Er on STO may promote the photocatalytic CO_2RR activities. On the other side, if RE single-atoms can be uniformly prepared on STO, the side contact with CN will build an electronic transfer tunnel to facilitate the interfacial charge separation, because the triazine structure of CN is easy to anchor Er.[36,39] Moreover, the ones outside the interface on STO nanoparticles will play a significant role in the activation of CO_2 molecules for accelerating the photocatalytic reaction.

Herein, this is the first report of single atom composite photocatalysts. Specifically, high dispersed Er single-atoms modified STO nanoparticles have successfully been obtained by in-situ doping method. The STO:Er^{3+} nanoparticles were then modified on the surface of CN nanosheets to prepare STO:Er^{3+}/CN nanocomposites. The Er single-atoms were confirmed by aberration-corrected high-angle annular dark-field scanning transmission electron microscopy (AC HAADF-STEM). The as-prepared STO:Er^{3+}/CN nanocomposites exhibited more than 5 times enhancement in photocatalytic CO_2RR compared to bulk g-C_3N_4 and $SrTiO_3$. By means of Er^{3+} fluorescence quenching, transient PL and DFT calculation, the promoted photoactivities were attributed to the dual-function role of the Er single-atoms which played as interfacial electronic transfer bridge and active site for CO_2 activation, so as to enhance the charge separation.

2. Experimental

The chemicals and characterization details are shown in Electronic Supplementary Information (ESI)†.

Synthesis of STO and STO:Er^{3+}. For STO, 1 mmol $Sr(NO_3)_2$ was dissolved in 19.67 mL PEG200 under vigorous stirring. Subsequently, 0.33 mL $Ti(OC_4H_9)_4$ and 22 mmol NaOH were added to the above solution, respectively. After being stirred, the mixture was transferred to autoclaves and maintained at 180 °C for 15 h. The final product was collected by centrifugation, washing with acetone, CH_3COOH, and deionized water, and drying in an oven at 70 °C. The synthesis process of STO:Er^{3+} is the same as that of STO, except adding $Er(NO_3)_3{\cdot}6H_2O$ into $Sr(NO_3)_2$ solution in the initial reaction stage. And the prepared STO:Er^{3+} composite was labeled as STO:Er^{3+}.

Synthesis of STO:Er^{3+}/CN. The CN was obtained by annealing melamine at 550 °C for 2 h under an N_2 atmosphere followed by a grinding treatment for subsequent experiments. A certain amount of CN was added into methanol and put in an ultrasonic bath for 3 h to make CN exfoliated completely. Then, different masses of STO:Er^{3+} are put into the above solution and kept ultrasonic for 30 min, finally stirred thoroughly until evaporated.

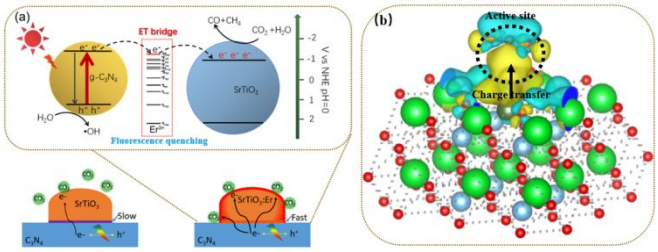

Fig. 1 (a, b) The proposed mechanism for Er^{3+} ions as ET bridge to promote charge separation thereby enhanced photocatalysis efficiency based on fluorescence quenching of Er^{3+} ions.

3. Results and discussion

3.1. Photocatalytic CO_2 reduction mechanism

In the proposed composite catalyst system (Fig. 1), the photoelectrons of CN were modulated by coupling STO as an appropriate platform for photoreduction of CO_2 by using visible light as an energy source. We achieved efficient photogenerated electron transfer from the conduction band of CN to STO and Er^{3+} ions are chosen as the ET bridge. As a bridge of ET, Er^{3+} ions must meet the following several conditions: (1) The energy level position of Er^{3+} ions as ET bridge should be in the middle of CN and STO conduction band positions. (2) The probability of nonradiative decay was found to be strongly dependent upon the proximity of lower energy levels. And thus, the position of the energy level as the ET bridge and the position of the lower level of rare-earth ions should be large enough to reduce the nonradiative transition probability inside energy levels of rare-earth ions. Here, it is noted that Er^{3+} is a very good upconversion activator (luminous center) rather than a good downconversion activator, so Er^{3+} is more suitable as an energy transfer bridge between STO and CN. (3) The radiation transition probability of inside energy levels of RE ions is as small as possible; thus, fluorescence quenching can occur. According to the bandgap structure of CN and STO, the $^4G_{11/2}$ energy level of Er^{3+} ions energy is the most suitable ET bridge. See supporting information for the explanation of the effect of the fluorescence quenching effect of Er^{3+} ions on the electron transfer from CN to STO. Of course, the lattice distortion of STO (Fig. S1†) caused by Er^{3+} doping will also affect the CO_2 adsorption capacity and catalytic performance of STO, which will be discussed in detail later. According to the mechanism

proposed above, the synthesis route of the composite system for promoting electron separation is shown in Fig. S2†, where STO:Er^{3+} and CN were separately synthesized first, and then STO:Er^{3+}/CN composites were obtained by chemical adsorption. The detailed synthesis information and sample abbreviation are stated in the ESI†.

3.2. Crystal structure and morphology properties

The particle size of the sample does not change obviously after doped with Er^{3+} because the concentration of Er^{3+} (only 3 mol%) is relatively low. The average particle size of STO or $SrTO_3$:Er^{3+} is about 10 nm, and the loading of small STO:Er^{3+} particles on the surface of CN was observed (Fig. 2 and Fig. S3-S4†). As shown in Fig. 2(d-f), the formation of erbium single atomic sites in STO:Er^{3+}/CN composite materials was confirmed by AC HAADF-STEM. The elemental mappings further indicate that the single erbium atoms are uniformly distributed on the STO nanoparticles surface (Fig. 2g). The results of XRD patterns indicate that STO and STO:3%Er^{3+} were pure perovskite oxides (Fig. S5†), and CN was a pure hexagonal phase (JCPDS 87-1526). When the concentration of Er^{3+} is more than 5 mol%, the diffraction peaks of impurity were observed. The characteristic peaks of CN and STO were detected in the composite sample, proving that a two-phase composition of CN and STO in 5-STO:Er^{3+}/CN sample.

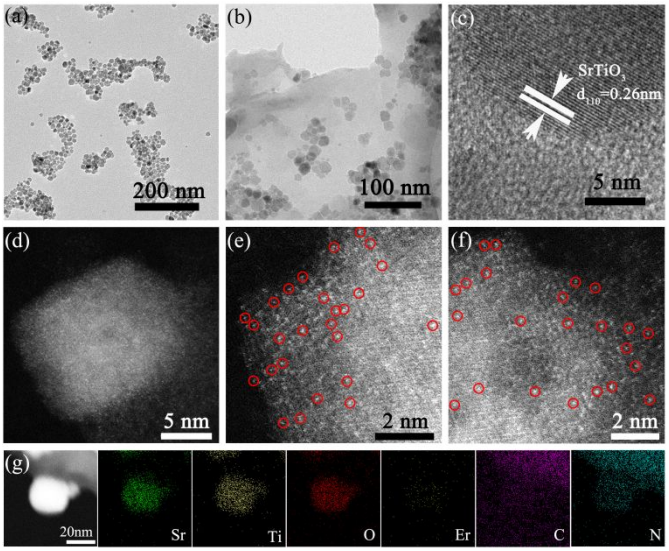

Fig. 2 TEM images of (a) STO:Er^{3+}, (b) 5-STO:Er^{3+}/CN. (c) HRTEM image of 5-STO:Er^{3+}/CN. (d-f) The AC HAADF-STEM images of 5-STO:Er^{3+}/CN. (g) HAADF-STEM image and EDX elemental mappings of 5-STO:Er^{3+}/CN.

The bandgap energies (Eg) of the CN, 5-STO:Er^{3+}/CN, 10-STO:Er^{3+}/CN, and STO:Er^{3+} are determined as approximately 2.64, 2.67, 2.70, and 3.16 eV, respectively (Fig. 3a). CN can exhibit visible light absorption while STO:Er^{3+} can only absorb ultraviolet light, and thus, the visible light catalytic performance of the composite is due to the absorption of light by CN first, then the electron transport to STO with the help of Er^{3+} as ET bridge, and finally the CO_2 reduction reaction takes place. It is worth noting that two very weak absorption peaks at 522 nm and 655 nm in the inset of Fig. 3a were assigned to the transitions from the ground $^4I_{15/2}$ state to the excited $^2H_{11/2}$ and $^4F_{9/2}$ states, respectively. The results show that the absorption of Er^{3+} ion is very weak and thus its contribution to the enhancement of visible light absorption of catalyst can be neglected, which further proves our proposed hypothesis above. In addition, the specific surface area of sample 5-STO:Er^{3+}/CN is increased compared to that of CN (Fig. 3b), showing that some molecule (such as CO_2) is beneficial to be adsorbed on the composite catalytic system surface, which is consistent with the above theoretical results.

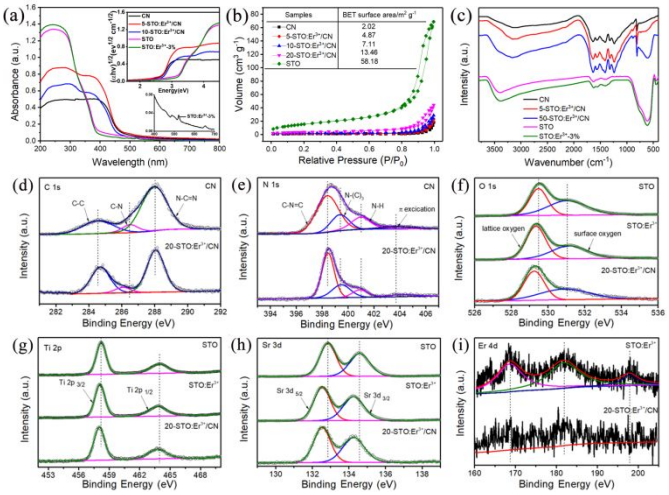

Fig. 3 (a) UV-vis diffuse reflectance spectra and band gaps patterns (inset), (b) N_2 adsorption-desorption isotherms, and (c) FT-IR spectra of different samples. (d-i) High-resolution XPS spectra of CN, STO, STO:Er^{3+}, and 20-STO:Er^{3+}/CN.

The FT-IR and XPS spectroscopy were used to investigate the interactions between CN and STO:Er^{3+} in composite materials (Fig. 3(c-i) and Fig. S6-S8†). The peak at 813 cm^{-1} in the FT-IR spectrum of pure CN corresponds to the characteristic breathing vibration of the s-triazine ring. The pure CN also shows the bands between 1200 cm^{-1} and 1700 cm^{-1}, which largely originate from the typical stretching vibration of CN heterocycles. The additional band at ~3100 cm^{-1} is the stretching vibration modes of NH and NH_2 groups, which is resulted from incomplete calcination of melamine on the surface of CN. For the STO, the absorption peak at around 3440 cm^{-1} could be caused by the hydroxyl groups on the sample surface. The broadband in the region from 500 cm^{-1} to 700 cm^{-1} corresponds to the Ti-O stretching vibrations. Note that the vibration peak of STO in the composites weakens, widens, and shifts, meaning that the surface doping of Er^{3+} on $SrTiO_3$ as well as the existence of interactions in the nanocomposites.

The XPS spectrum of C 1s for CN can be split into three peaks at 284.6, 286.5, and 288.0 eV attributed to the C-C, C-N, and N=C-N (Fig. 3d). However, the peaks at 284.7, 286.1, and 288.1 eV were observed for 20-STO:Er^{3+}/CN, indicating the increased electronic density of C surface and the existence of an interaction between STO:Er^{3+} and CN. For the N 1s XPS spectra of CN, the observed four peaks at 398.4, 399.4, 401.0, 403.8 eV were ascribed to the sp2-hybridized nitrogen atoms (C=N-C),

bridging nitrogen atoms (C_3-N), the N-H bonding and the charging effects caused by π-excitations. For 20-STO:Er^{3+}/CN, the peaks of N-$(C)_3$ and π-excitations were shifted to 399.5 and 403.1 eV, proving the existence of an interaction between STO:Er^{3+} and CN (Fig. 3e). The peaks at 529.5 and 531.1 eV in the O 1s spectrum of STO correspond to the lattice oxygen O^{2-} species and surface oxygen, respectively (Fig. 3f). While the combined energy of lattice oxygen O^{2-} species shifts to low energy direction after Er^{3+} doping or CN coupling. The Ti 2p spectrum can be divided into two parts with peaks at 458.2 eV and 464.0 eV in STO (Fig. 3g), which corresponds to Ti $2p_{3/2}$ and Ti $2p_{1/2}$, respectively. In 20-STO:Er^{3+}/CN and STO:Er^{3+} samples, the two peaks are located at 458.0 eV and 463.8 eV, respectively. The Sr spectrum in pure STO is primarily composed of two binding energy peaks of Sr $3d_{5/2}$ and Sr $3d_{3/2}$ at 132.9 eV and 134.6 eV (Fig. 3h). Compared with STO, the binding energy of Sr 3d peaks of 20-STO:Er^{3+}/CN and STO:Er^{3+} shifts to a lower energy direction, which is due to the fact that Er^{3+} ion doping changes the local electronic structure. The peaks in Fig. 3i is attributed to Er 4d. The XPS valence band of STO and STO:Er^{3+} is at 2.19 and 2.13 eV, respectively (Fig. S7†). The position shift of binding energy in STO proves the change of electronic density as well as the existence of an interaction between STO:Er^{3+} and CN. The Er^{3+} concentration in the STO:Er^{3+} and 20-STO:Er^{3+}/CN samples is 2.5816% and 0.3293% mg/L, respectively, which was measured by using ICP-OES technology.

3.3. Photocatalytic activity and charge separation

To confirm the photocatalytic mechanism described above, the performance of photocatalytic reduction of CO_2 for STO, STO:Er^{3+}, CN, and STO:Er^{3+}/CN has been studied in detail (Fig. 4(a-d)). As shown in Fig. 4a, STO:Er^{3+} exhibits a higher CO and CH_4 evolution rate than STO under ultraviolet light. This result shows that the exposed Er^{3+} ions on the surface can effectively activate CO_2 to improve photocatalytic activity. Next, we studied the CO_2 reduction performance of the photocatalyst under visible light irradiation. As shown in Fig. 4b, 5-STO:Er^{3+}/CN shows a CO-evolution rate of 22.35 μmol g^{-1} h^{-1} and a CH_4-evolution rate of 16.90 μmol g^{-1} h^{-1} in a mixed system of acetonitrile, water and triethanolamine. And compared with pure CN, the maximum production rate of CO and CH_4 can be increased by about 5 times. The performance comparison of all the rare earth single atom photocatalysts reported is summarized in Table 1. It is noted that the yield of CH_4 is more important than that of CO during the process of CO_2RR, so the performance of 5-STO:Er^{3+}/CN in this work is quite good. Of course, it is noted that not all RE ions are suitable for charge transfer bridges because the role of RE ions is not only related to the structure of RE ions but also related to the properties of $SrTiO_3$ and g-C_3N_4. So, there is still a lot of room for improvement in the design of RE single atom composite photocatalysts. We also further studied the photocatalytic CO_2 reduction ability of CN, 5-STO/CN and x-STO:Er^{3+}/CN (x=1, 3, 5, 7, and 10) photocatalysts in the pure water system. As predicted, the 5-STO:Er^{3+}/CN sample shows the excellent CO evolution rate of 5.68 μmol h^{-1} g^{-1} and CH_4 production rate of 2.30 μmol g^{-1} h^{-1}, which is approximately 2 folds higher than that of pure CN (Fig. 4c). However, the introduction of excessive STO:Er^{3+} will cause a decrease in photocatalytic CO_2 reduction activity, indicating that the introduction of STO:Er^{3+} can improve the photocatalytic activity of CN, but the proper amount of STO:Er^{3+} is important because STO can only absorb UV light and excess STO will lead to the decrease of CN. The photoactivity of 5-STO/CN in the absence of Er^{3+} is lower compared to the corresponding samples containing Er^{3+}, and this further proves that partial Er^{3+} ions can act as an energy transfer bridge between STO and CN to promote charge separation. In addition, after three consecutive photocatalytic tests, 5-STO:Er^{3+}/CN still maintained excellent CO_2 photoreduction stability (Fig. 4d). To further confirm the source of the produced CH_4, we carried out an isotopic experiment using CO_2 under identical photocatalytic reaction conditions. The photocatalytic evolution of CH_4 was analyzed by gas chromatography mass (GC-MS), of which the peak m/z = 17 is assigned to CH_4 and the fragment ion of CH_4 is seen as well as shown in Fig. S9†.

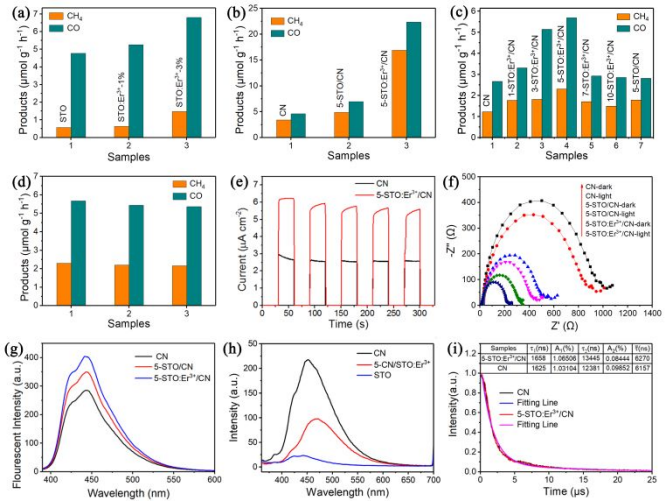

Fig. 4 (a) The photocatalytic production amount of STO, STO:Er^{3+}-1%, and STO:Er^{3+}-3% under ultraviolet light irradiation (pure water system). (b) The photocatalytic production amount of CN, 5-STO/CN, and 5-STO:Er^{3+}/CN under visible light irradiation with TEOA as sacrificial agent for photocatalytic reaction. (c) The photocatalytic production amount of CN, x-STO:Er^{3+}/CN (x=1, 3, 5, 7, and 10), and 5-STO/CN under visible light irradiation (pure water system). (d) Evaluation of the stability of 5-STO:Er^{3+}/CN under visible light irradiation (pure water system). (e) Photocurrent responses, (f) EIS spectra, (g) Fluorescence spectra related to the produced hydroxyl radicals under visible-light irradiation, (h) PL spectra under the excitation wavelength of 350 nm, and (i) Luminescence decay curves.

Table 1. Comparison of visible-light photocatalytic performance for also the rare earth single atom photocatalysts reported.

Single atom photocatalysts	Sacrificial agent	Catalytic Performance (μmol/h/g)		References
		CO	CH_4	
g-C_3N_4:Er	Without	47.1	2.5	Ref. 36
g-C_3N_4:La	TEOA	92	5.6	Ref. 37
$SrTiO_4$:Er/g-C_3N_4	TEOA	22.35	16.9	This work

The photocurrent generation behavior (Fig. 4e) shows that much higher photocurrent is obtained from the 5-STO:Er^{3+}/CN sample than that of pristine CN, indicating 5-STO:Er^{3+} can greatly improve the separation efficiency of photogenerated carriers.[40] Moreover, the photocurrents of the two samples are reproducible and stable, indicating the photostability of the samples is good. The electrochemical impedance spectra (EIS) Nyquist plots of pristine CN, STO/CN, and 5-STO:Er^{3+}/CN are shown in Fig. 4f and the smallest arc radius was obtained from 5-STO:Er^{3+}/CN. This means that photogenerated electron-hole pairs are more effectively separated and charges are more efficiently immigrated across the electrode/electrolyte interface in 5-STO:Er^{3+}/CN. Thus 5-STO:Er^{3+}/CN can greatly enhance the photogenerated electron-hole separation and transfer. Moreover, both the separated photogenerated electrons and holes increase hydroxyl radicals (·OH) via redox of H^+ and H_2O, thus the electron-hole separation can also be evaluated by measuring the concentration of ·OH.[41] We measured fluorescence spectra of luminescent 7-hydroxycoumarin produced from the reaction between and ·OH and coumarin by using the coumarin fluorescent method. A a general rule, more hydroxyl radical generation results in stronger fluorescent signal. We observed the highest intensity from 5-STO:Er^{3+}/CN sample as shown in Fig. 4g, which means introducing STO:Er^{3+} significantly improved photogenerated charge separation. Furthermore, the PL intensity has been widely used as a measure of charge recombination rate and the higher PL intensity indicates a higher recombination rate. We observe the lower PL intensity from 5-STO:Er^{3+}/CN compared to that of pristine CN as shown in Fig. 4h. This further proves that introducing STO:Er^{3+} can effectively reduce electron-hole recombination. In addition, the emission peaks of Er^{3+} cannot be detected, indicating that the fluorescence quenching effect of Er^{3+} ions was observed (Fig. 1a). The average lifetime of the photogenerated carrier for CN and 5-STO:Er^{3+}/CN was calculated as 6157 ns and 6270 ns, respectively, which further proves it is more effective to generate and separate electron-hole pairs in 5-STO:Er^{3+}/CN sample (Fig. 4i).

3.4. DFT calculation and discussion

To further study the rationality of the charge separation system designed, suitable lattice structures of STO, $ErTiO_3$ (ETO), and CN were selected and optimized by using DFT (Fig. 5, Fig. S10†, and Table S1†). Both the STO and ETO are semiconductors with an indirect bandgap energy of 3.16 and 2.30 eV, and direct bandgap energy of 3.54 and 2.71 eV, respectively. Thus, the bandgap energy of Er-doped STO could be engineered by tuning the ratio of Er to Sr, which is consistent with our experimental results. For both $SrTiO_3$ and $ErTiO_3$, the CBs are mainly contributed by the orbitals of Ti atoms, and the VBs are mainly contributed by the orbitals of O atoms. The replacement of Sr with Er significantly lowered the CB minimum while no obvious change of VB maximum was observed.

The theoretical simulation results of the differential charge density and electron localization function (ELF) in Fig. 6 showed that the net charge on Ti and O is 2.65 and -1.44, respectively in $SrTiO_3$, while the net charge on Ti and O is 2.40 and -1.26, respectively in $ErTiO_3$. This indicates that the replacement of Sr with Er affects the interactions between Ti and O. Compared with $SrTiO_3$, the interaction between Ti and O is stronger, and Ti loses fewer electrons, therefore, the bandgap of $ErTiO_3$ is smaller than that of $SrTiO_3$. The doping of Er into $SrTiO_3$ introduced additional energy levels between CB minimum of CN and $SrTiO_3$ and these additional energy levels serve as energy transfer bridges for the ease of electron transfer from CN to $SrTiO_3$.

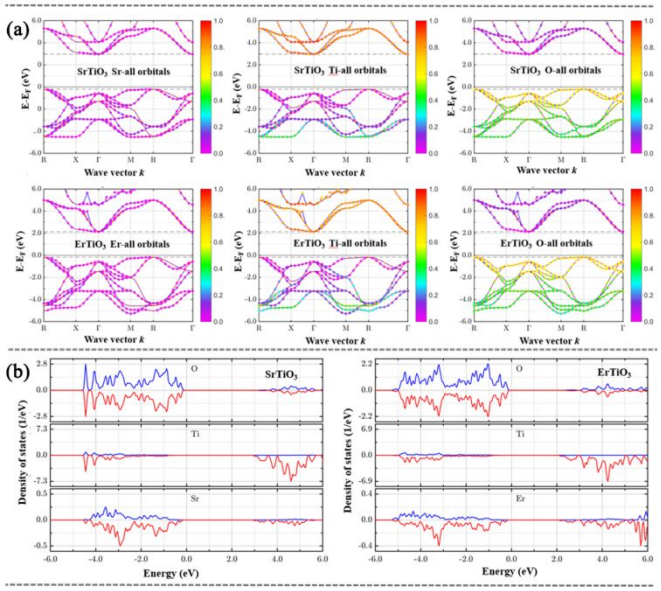

Fig. 5 (a) The band structure (BS) and (b) the density of states (DOS) contributed by each element of $SrTiO_3$ and $ErTiO_3$.

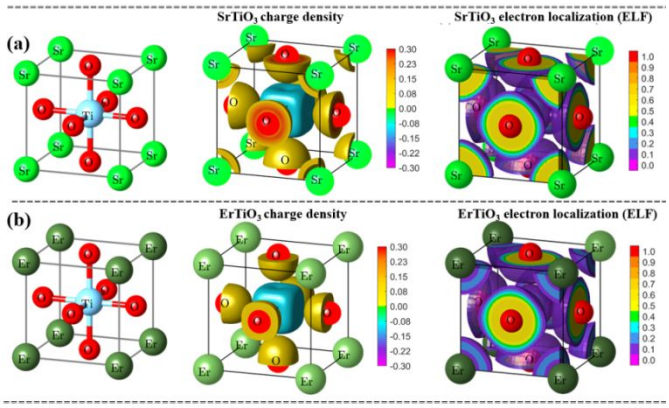

Fig. 6 Theoretical simulation results of the charge density and electron localization: (a) $SrTiO_3$ and (b) $ErTiO_3$.

The results of theoretical simulation in Fig. S11† show that the electronic structure and optical properties of $SrTiO_3$ and $ErTiO_3$ are different. The absorption coefficient of $ErTiO_3$ is larger than that of $SrTiO_3$ in the visible region, which indicates that doping Er into $SrTiO_3$ might also increase the light absorption capability. Furthermore, the optical conductivity of $ErTiO_3$ shows better optical conductivity than that of $SrTiO_3$. Thus, doping Er into $SrTiO_3$ also increases the charge transfer and separation. Therefore, the substitution of Er^{3+} for Sr^{2+} lattice in $SrTiO_3$ will give some novel properties to the $SrTiO_3$,

which is expected to improve the photocatalytic activity of $SrTiO_3$.

As mentioned above, the lattice parameters, work functions, adsorption capacity of CO_2 on the surface of STO, and charge density difference are changed through Er^{3+} doping (Fig. 7 and Fig. S12-S13†). The thickness of the vacuum layer is 10 Å. The work functions of STO (001), STO:Er^{3+} (001), STO (110), STO:Er^{3+} (110), and CN (001) are 3.64, 2.74, 5.82, 5.97, and 4.22 eV, respectively. The work function of CN (001) is greater than that of STO (001) and STO:Er^{3+} (001) while less than that of STO (110) and STO:Er^{3+} (110). The adsorption energy of CO_2 on the surface of STO (110) and CN (001) are 5.82 and 4.22 eV, respectively. The charge differential density shows that Er^{3+} not only can result in the change of the density of the surrounding electron cloud but also can better absorb CO_2 and play the role of activation center.[33] All these theoretical results further prove that the composite system proposed is conducive to promoting charge separation and improving photocatalytic activity.

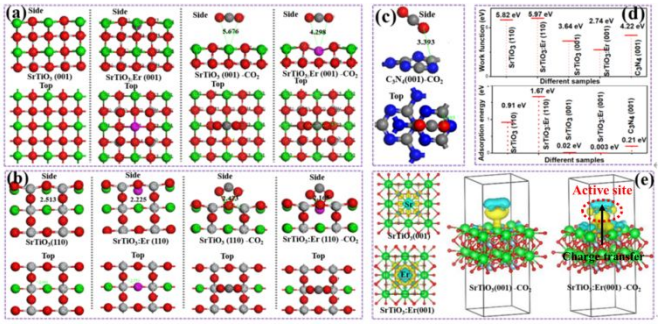

Fig. 7 (a-c) Side and top view of the optimized crystal structure and CO_2 adsorption on the different surfaces of STO, STO:Er^{3+}, and CN. (d) The calculated work function and adsorption energy (the Fermi energy is used as the zero of the energy scale). (e) The effect Er^{3+} on the charge density difference around Er^{3+} in STO:Er^{3+} (001) as well as CO_2 in CO_2-STO:Er^{3+} (001). In (e), the yellow and cyan surfaces correspond to the charge gain and charge loss, respectively.

4. Conclusions

In conclusion, the mechanism proposed in this work is based on fully considering the characteristics of narrow half peak width and low luminous efficiency of rare-earth single-atoms, breaking through the traditional view that RE ions are used as light conversion agents, and realizing the dual effects of erbium ions activating CO_2 and acting as an energy transfer bridge to promote charge separation. The formation of Er single-atoms in STO:Er^{3+}/CN composite material was confirmed by AC HAADF-STEM. The results of UV-vis DRS, EIS, and XPS show that the surface doping of single-atoms Er^{3+} on $SrTiO_3$ favors building an energy transfer bridge between SrTiO3 and g-C_3N_4, resulting in the enhanced interfacial charge separation. A series of calculation results of band structure, work function, and CO_2 adsorption energy prove that the STO:Er^{3+} surface serves as dual functional roles of charge separation and CO_2 activation to promote the photocatalytic activity of CO_2RR. As expected, the experiment results indicate that STO:Er^{3+}/CN exhibits much higher photocatalytic performance under visible light irradiation compared to that of pristine g-C_3N_4 and STO/CN. This provides a new way of thinking and perspective for the development of highly efficient photocatalytic materials modified by RE single-atoms.

Author contributions

Q. C. and G. G. analyzed the experimental data and wrote original draft. Q. C., G. G., Y. Z. and Y. L. performed major experiments. G. W., H. Z., Q. C. and G. G. designed the concept of this work. G.W., H. Z. and P. Z. performed the computational study. G.W., H. Z., W. Q. and Y. Q revised the manuscript. All the authors discussed the results and commented on the manuscript.

Conflicts of interest

There are no conflicts to declare.

Acknowledgments

This work was supported by the National Natural Science Foundation of China (No. 21871079 and 11774128), the National Science Foundation (No. 1945558), the Outstanding Youth Project of Natural Science Foundation of Heilongjiang Province (YQ2019B006 and LBH-Q19052), and the Natural Science Foundation of Shandong Province (ZR2018JL003, 2019KJJ003).

Notes and references

1 J. Ran, M. Jaroniec and S. Qiao, *Adv. Mater.*, 2018, **30**, 1704649.
2 G. Wang, C. He, R. Huang, J. Mao, D. Wang and Y. Li, *J. Am. Chem. Soc.*, 2020, **142**, 19339-19345.
3 X. Jiao, K. Zheng, Z. Hu, Y. Sun and Y. Xie, *ACS Central Sci.*, 2020, **6**, 653-660.
4 C. Chen, W. Ma and J. Zhao, *Chem. Soc. Rev.*, 2010, **39**, 4206-4219.
5 L. Ji, L. Li, X. Ji, Y. Zhang, S. Mou, T. Wu, Q. Liu, B. Li, X. Zhu, Y. Luo, X. Shi, A. M. Asiri and X. Sun, *Angew. Chem. Int. Ed.*, 2020, **59**, 758-762.
6 H. Zhang, P. Zhang, M. Qiu, J. Dong, Y. Zhang and X. W. Lou, *Adv. Mater.*, 2019, **31**, 1804883.
7 M. F. Kuehnel, K. L. Orchard, K. E. Dalle and E. Reisner, *J. Am. Chem. Soc.*, 2017, 139, 7217-7223.
8 H. Mao, Z. Jin, F. Zhang, H. He, J. Chen and Y. Qian, *Ceram. Int.*, 2018, 44, 17535-17538.
9 Y. Jiang, H. Chen, J. Li, J. Liao, H. Zhang, X. Wang and D. Kuang, *Adv. Funct. Mater.*, 2020, **30**, 2004293.
10 Y. A. Wu, I. McNulty, C. Liu, K. C. Lau, Q. Liu, A. P. Paulikas, C. Sun, Z. Cai, J. R. Guest, Y. Ren, V. Stamenkovic, L. A. Curtiss, Y. Liu and T. Rajh, *Nat. Energy*, 2019, **4**, 957-968.
11 H. Zhang, Y. Wang, S. Zuo, W. Zhou, J. Zhang and X. W. Lou, *J. Am. Chem. Soc.*, 2021, **143**, 2173-2177.

12 J. Shen, Y. Li, H. Zhao, K. Pan, X. Li, Y. Qu, G. Wang and D. Wang, *Nano Res.*, 2019, **12**, 1931-1936.
13 X. Liu, S. Xu, H. Chi, T. Xu, Y. Guo, Y. Yuan and B. Yang, *Chem. Eng. J.*, 2019, **359**, 1352-1359.
14. Y. Dai, C. Li, Y. Shen, T. Lim, J. Xu, Y. Li, H. Niemantsverdriet, F. Besenbacher, N. Lock and R. Su, *Nat. Commun.*, 2018, **9**, 60.
15 T. Xiong, W. Cen, Y. Zhang and F. Dong, *ACS Catal.*, 2016, **6**, 2462-2472.
16 Z. Jiang, W. Wan, H. Li, S. Yuan, H. Zhao and P. K. Wong, *Adv. Mater.*, 2018, **30**, 1706108.
17 F. Yang, X. Chua, J. Sun, Y. Zhang, Z. Li, H. Liu, L. Bai, Y. Qu and L. Jing. *Chinese Chem. Lett.*, 2020, **31**, 2784-2788.
18 R. Kuriki, M. Yamamoto, K. Higuchi, Y. Yamamoto, M. Akatsuka, D. Lu, S. Yagi, T. Yoshida, O. Ishitani and K. Maeda, *Angew. Chem. Int. Ed.*, 2017, **56**, 4867-4871.
19 B. Ma, G. Chen, C. Fave, L. Chen, R. Kuriki, K. Maeda, O. Ishitani, T.-C. Lau, J. Bonin and M. Robert, *J. Am. Chem. Soc.*, 2020, **142**, 6188-6195.
20 J. Fu, B. Zhu, C. Jiang, B. Cheng, W. You and J. Yu, *Small*, 2017, **13**, 1603938.
21 H. Pan, Y.-W. Zhang, V. B. Shenoy and H. Gao, *ACS Catal.*, 2011, **1**, 99-104.
22 W.J. Ong, L.L. Tan, Y. H. Ng, S.-T. Yong and S.P. Chai, *Chem. Rev.*, 2016, **116**, 7159-7329.
23 Y.-C. Pu, H.-C. Fan, T.-W. Liu and J.-W. Chen, *J. Mater. Chem. A*, 2017, **5**, 25438-25449.
24 H. Shi, G. Chen, C. Zhang and Z. Zou, *ACS Catal.*, 2014, **4**, 3637-3643.
25 L. Jiang, K. Wang, X. Wu and G. Zhang, *Solar RRL*, 2021, **5,** 2000326.
26 Y. Wang, L. Guo, Y. Zeng, H. Guo, S. Wan, M. Ou, S. Zhang and Q. Zhong, *ACS Appl. Mater. Interfaces*, 2019, **11**, 30673-30681.
27 P. Ding, H. Zhao, T. Li, Y. Luo, G. Chen, S. Gao, X. Shi, S. Lu and X. Sun, *J. Mater. Chem. A*, 2020, **8**, 21947-21960.
28 Z. Zhang, L. Bai, Z. Li, Y. Qu and L. Jing, *J. Mater. Chem. A*, 2019, **7**, 10879-10897.
29 T. Kanagaraj and S. Thiripuranthagan, *Appl. Catal. B-Environ.*, 2017, **207**, 218-232.
30 Q. Yang, C. Yang, C. Lin and H. Jiang, *Angew. Chem. Int. Ed.*, 2019, **58**, 3511-3515.
31 C. Gao, S. Chen, Y. Wang, J. Wang, X. Zheng, J. Zhu, L. Song, W. Zhang and Y. Xiong, *Adv. Mater.*, 2018, **30**, 1704624.
32 Y. Li, B. Li, D. Zhang, L. Cheng and Q. Xiang, *ACS Nano*, 2020, **14**, 10552-10561.
33 J. Wang, T. Heil, B. Zhu, C.-W. Tung, J. Yu, H. M. Chen, M. Antonietti and S. Cao, *ACS Nano*, 2020, **14**, 8584-8593.
34 R. Sun, Y. Liao, S.-T. Bai, M. Zheng, C. Zhou, T. Zhang and B. F. Sels, Energy & Environmental Science, 2021, 14, 1247-1285.
35 C. Chen, Y. Li, D. Cheng, H. He and K. Zhou, *ACS Appl. Mater. Interfaces*, 2020, 12, 40415-40425.
36 S. Ji, Y. Qu, T. Wang, Y. Chen, G. Wang, X. Li, J. Dong, Q. Chen, W. Zhang, Z. Zhang, S. Liang, R. Yu, Y. Wang, D. Wang and Y. Li, *Angew. Chem. Int. Ed.*, 2020, **59**, 10651-10657.
37 P. Chen, B. Lei, X. a. Dong, H. Wang, J. Sheng, W. Cui, J. Li, Y. Sun, Z. Wang and F. Dong, *ACS Nano*, 2020, **14**, 15841-15852.
38 J. Liu, X. Kong, L. Zheng, X. Guo, X. Liu and J. Shui, *ACS Nano*, 2020, **14**, 1093-1101.
39 X. Li, K. Pan, Y. Qu and G. Wang, *Nano Res.*, 2018, **11**, 1322-1330.
40 H. Dong, X. Zhang, Y. Lu, Y. Yang, Y. Zhang, H. Tang, F. Zhang, Z. Yang, X. Sun and Y. Feng, *Appl. Catal. B-Environ.*, 2020, **276**, 119173.
41 J. Sun, J. Bian, J. Li, Z. Zhang, Z. Li, Y. Qu, L. Bai, Z.-D. Yang and L. Jing, *Appl. Catal. B-Environ.*, 2020, **277**, 11919.